Pergamon

Int. J. Solids Structures Vol. 33, No. 24, pp. 3497–3516, 1996

0020-7683/96 $15.00 + .00

0020-7683(95)00198-0

EFFECT OF EXTRINSIC AND INTRINSIC FACTORS ON AN INDENTATION TEST

SRINATH TRIMULA, HARIKRISHNA MADANARAJ, AUTAR K. KAW*, GLEN H. BESTERFIELD and JIAFEI YE

Department of Mechanical Engineering, University of South Florida, Tampa, Florida 33620-5350, U.S.A.

(*Received* 27 *April* 1995; *in revised form* 14 *August* 1995)

Dedication—To our dearest friends and graduate students, Indeevar Lanka and Srinath Tirumala, who are no more with us. They were the pedestal of academic support and help during this course of study in the university.

Abstract—The effect of intrinsic and extrinsic factors on the measured results, such as load–displacement curves and interfacial stresses, from indentation tests of composite materials is studied using both analytical and finite element models. The intrinsic factors include properties of the fiber-matrix interface and the material symmetry of the fiber (transversely isotropic or isotropic). The extrinsic factors include the radius of the hole through which the fiber is pushed in, and the size and shape of the indentor. Out of the above factors, only the radius of the hole is found to have a negligible effect on the results of the indentation test. Copyright © 1996 Elsevier Science Ltd.

INTRODUCTION

The interface is a very vital aspect of a ceramic matrix composite in determining its strength and fracture toughness. Hence, the quantitative measurement of the mechanical properties of the interface between the fiber and matrix in such composites is of great importance.

The tests most often used to measure interface properties in ceramic matrix composites are indentation tests (Marshall, 1984). Lawrence and Derby (1993) conducted fiber push-through experiments using a nano-indentor to examine the interfacial shear strengths of ceramic matrix composites. They concluded that Poisson's ratio plays an important part in determining the shear strengths. Curtin *et al.* (1993) performed fiber push-in tests on a ceramic matrix composite consisting of carborundum sintered SiC fibers, with a BN coating, embedded in a reaction bonded SiC matrix. They found out that these coatings provide the necessary debonding and sliding characteristics required for good composite behavior. They also found that the rough surface of these fibers did not cause either substantial mechanical interlocking or inhibited sliding in this system.

As experiments become expensive and iterative, and analytical models become untractable, emphasis has shifted towards simulating experiments using finite element methods. The primary advantage of a finite element simulation is that it is time efficient and can be simulated close to the actual experimental set up. Material properties, loads, and boundary conditions can be easily changed to study the effects of various parameters. Hence, several studies using finite element analysis have been made to study the interfacial properties.

Faber *et al.* (1986) used a finite element algorithm developed for frictional contact problems to evaluate the frictional stresses and displacements, during fiber push-in. Their results showed that the displacements asymptotically decayed to the "perfectly" bonded condition as the coefficient of friction increased, and the interfacial shear stress and shear stress gradient increased with an increasing coefficient of friction.

Shirazi-Adi (1992) developed inter-element stress compatible elements to perform the push-in test. The formulation of the continuity of the interfacial stresses was enforced by a penalty procedure. Axial compressive forces and axial torques were both considered. His results indicated a complex state of interfacial stresses where the variation of interfacial

* To whom correspondence should be addressed.

shear stress is highly non-uniform and the radial interfacial stresses are likely to be large.

Meda *et al.* (1993) used an integral equation method, as well as a finite element method, to simulate the indentation test to investigate the effect of fiber Poisson's ratio on the interfacial stresses, displacements and slip lengths. They predicted that the load required to produce a given slip length is larger when the shear stress depends on the normal stress than when the shear stress is assumed to have a constant value. This is because the effect of Poisson's ratio mismatch between the fiber and matrix is accounted for during slippage in the former case.

Recent experimental results by Koss *et al.* (1993) on related thin-slice push-in tests suggest that the interfacial failure processes are dependent on specimen configuration and thermally induced residual stresses, as well as the interfacial bond strength and toughness, matrix plasticity, coefficient of friction, and Poisson's ratio.

The objective of this work is to analytically and numerically study the effects of intrinsic and extrinsic factors on the results of indentation tests. Analytical models study the effect of the shape and size of the indentors, for frictional and perfectly bonded interfaces. The finite element study includes the effects of the radius of the hole through which the fiber is pushed in, shape and size of the indentor, ratio of fiber to matrix Young's moduli, and material symmetry (isotropic and transversely isotropic properties) of the fiber on the indentation tests.

MODELING BACKGROUND

For the indentation test, a composite is sliced normal to the fiber direction and the specimen is placed on a platform with a hole as shown in Fig. 1. A micro-indentor with a radius which is 60–90% of the radius of the fiber pushes on the fiber. The indentation load on the fiber and the displacement on the surface of the fiber below the matrix surface due to interfacial slip is measured to construct a load–displacement curve. The load–displacement curve from the test can then be compared to those obtained through analytical models to determine interfacial properties such as the residual interfacial stress and coefficient of friction.

One such analytical model is given by Shetty (1988). He gave simple equations for the indentor load, P, and the relative displacement at the interface, Δu_z, between the fiber and the matrix at the top free surface. These relations are given as:

$$\frac{P}{\pi b^2} = \frac{\sigma_0}{k}\left[\exp\left(\frac{2\mu k L_s}{b}\right) - 1\right] \tag{1a}$$

$$\frac{\Delta u_z}{b} = \frac{(1-2\nu_f k)\sigma_0}{kE_f}\left\{\frac{1}{2\mu k}\left[\exp\left(\frac{2\mu k L_s}{b}\right) - 1\right] - \frac{L_s}{b}\right\} \tag{1b}$$

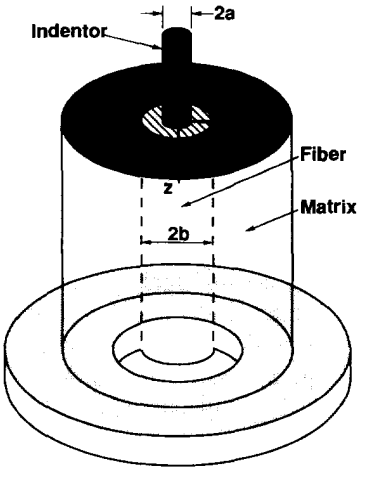

Fig. 1. Composite specimen on an annular platform for an indentation test.

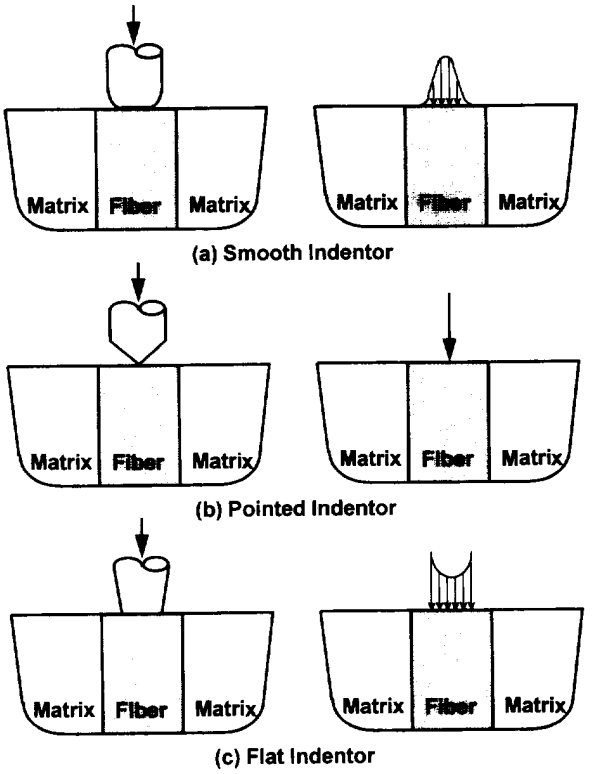

Fig. 2. Various indentor geometries and the approximated pressure distributions on the fiber.

respectively, where μ is the friction coefficient, σ_0 is the residual compressive stress at the interface prior to loading, b is the fiber radius, L_s is the slip length, and k is defined by

$$k = \frac{E_m v_f}{E_f(1+v_m)+E_m(1-v_f)}. \tag{2}$$

where E_f, v_f, E_m, v_m are the Young's moduli and Poisson's ratios for fiber and matrix, respectively. If the displacements are measured for several indentor loads in an indentation test, eqns (1a,b) can be used to find the interfacial properties, such as, interfacial coefficient of friction, μ, and residual compressive stress, σ_0.

Since load-displacement curves are critical in determining interfacial properties from an indentation test, an analytical and numerical study is presented here to study the effect of both extrinsic and intrinsic factors on the curve. Furthermore, the effect on the interfacial stresses is also studied. The extrinsic factors include:

—indentor shape (see Fig. 2),
  —smooth—round indentor (Grande *et al.*, 1988)
  —pointed—Vicker's pyramid indentor (Marshall, 1984)
  —flat—carbide tool indentor (Bright *et al.*, 1991)
—indentor size (ratio of indentor radius to fiber radius), and
—push through hole radius.

The intrinsic factors studied include:

—relative elastic moduli of fiber and matrix and
—material symmetry of fiber.

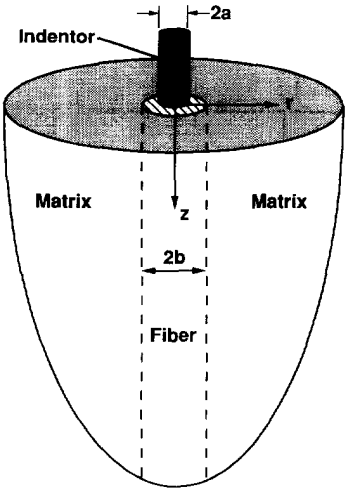

Fig. 3. Circular fiber embedded in an infinite half plane under an indentor load.

ANALYTICAL MODELS

Analytical model 1

A circular fiber embedded in an infinite half-space, as shown in Fig. 3, is considered. The fiber and the matrix are assumed to have the same elastic modulus and are perfectly bonded. An axisymmetric, but arbitrary, pressure over an arbitrary area is applied on the fiber. This model is used to study the effect of indentor shape and size on the maximum interfacial stresses and axial displacements at the fiber-matrix interface at $z = 0$.

Geometry. The geometry of this model is shown in Fig. 3. A semi-infinite circular fiber of radius, b, is bonded to a half space of inner radius, b, and infinite outer radius. Young's modulus and the Poisson's ratio of the fiber and the matrix are equal and are denoted as E and ν, respectively.

Boundary conditions. The fiber and the matrix are perfectly bonded, that is,

$$u_r^f(b,z) = u_r^m(b,z), \quad 0 < z < \infty \tag{3a}$$

$$u_z^f(b,z) = u_z^m(b,z), \quad 0 < z < \infty \tag{3b}$$

$$\sigma_{rr}^f(b,z) = \sigma_{rr}^m(b,z), \quad 0 < z < \infty \tag{3c}$$

$$\sigma_{rz}^f(b,z) = \sigma_{rz}^m(b,z), \quad 0 < z < \infty \tag{3d}$$

At $z = 0$, only the fiber is subjected to a pressure, $p(r)$, over a radius, a, that is,

$$\sigma_{zz}^f(r,0) = -p(r), \quad 0 < r < a < b \tag{4a}$$

$$\sigma_{zz}^f(r,0) = 0, \quad a < r \leqslant b \tag{4b}$$

$$\sigma_{zz}^m(r,0) = 0, \quad b \leqslant r < \infty \tag{4c}$$

Furthermore, on the surface ($z = 0$), the shear stress is zero, that is,

$$\sigma_{rz}^f(r,0) = 0, \quad 0 \leqslant r \leqslant b \tag{5a}$$

$$\sigma_{rz}^m(r,0) = 0, \quad b \leqslant r < \infty \tag{5b}$$

The pressure, $p(r)$, and loading radius, a, are arbitrary, where the pressure, $p(r)$, is

dependent on the indentor shape. The pressure distribution for common indentors (see Fig. 2) is assumed as

$$p(r) = \frac{P}{2\pi a\sqrt{a^2-r^2}}, \quad 0 \leqslant r < a, \quad \text{(flat indentor)} \tag{6a}$$

$$p(r) = \frac{3P}{2\pi a^3}\sqrt{a^2-r^2}, \quad 0 \leqslant r < a, \quad \text{(smooth indentor)} \tag{6b}$$

$$p(r) = P\delta(0), \quad \text{(pointed indentor)} \tag{6c}$$

where the load, P, is the overall load applied to the indentor, and is given as

$$P = \int_0^{2\pi}\int_0^a p(r) r \, dr \, d\theta \tag{7}$$

and $\delta(0)$ is the Dirac delta function.

Also, in many analytical studies, a uniform pressure distribution is used to approximate the indentor load. The pressure, $p(r)$, in this case is assumed of the form

$$p(r) = \frac{P}{\pi a^2}, \quad 0 \leqslant r < a, \quad \text{(uniform pressure)} \tag{8}$$

Method of analysis. This problem is the classical Terezawa's solution for a semi-infinite medium (Sneddon, 1951). The solution for the displacements and stresses in the fiber as well as the matrix are given as

$$u_r(r,z) = \frac{z}{2G}\int_0^a tp(t) I_{011}(r,z,t)\,dt - \frac{1}{2(\lambda+G)}\int_0^a tp(t) I_{010}(r,z,t)\,dt \tag{9}$$

$$u_z(r,z) = \frac{z}{2G}\int_0^a tp(t) I_{001}(r,z,t)\,dt + \frac{\lambda+2G}{2G(\lambda+G)}\int_0^a tp(t) I_{000}(r,z,t)\,dt \tag{10}$$

$$\sigma_{rr}(r,z) = -\int_0^a tp(t) I_{001}(r,z,t)\,dt + z\int_0^a tp(t) I_{002}(r,z,t)\,dt - \frac{z}{r}\int_0^a tp(t) I_{011}(r,z,t)\,dt + \frac{G}{r(\lambda+G)}\int_0^a tp(t) I_{010}(r,z,t)\,dt \tag{11}$$

$$\sigma_{zz}(r,z) = -z\int_0^a tp(t) I_{002}(r,z,t)\,dt - \int_0^a tp(t) I_{001}(r,z,t)\,dt \tag{12}$$

$$\sigma_{\theta\theta}(r,z) = -\frac{\lambda}{\lambda+G}\int_0^a tp(t) I_{001}(r,z,t)\,dt - \frac{G}{r(\lambda+G)}\int_0^a tp(t) I_{010}(r,z,t)\,dt + \frac{z}{r}\int_0^a tp(t) I_{011}(r,z,t)\,dt \tag{13}$$

$$\sigma_{rz}(r,z) = -z\int_0^a tp(t) I_{012}(r,z,t)\,dt \tag{14}$$

where

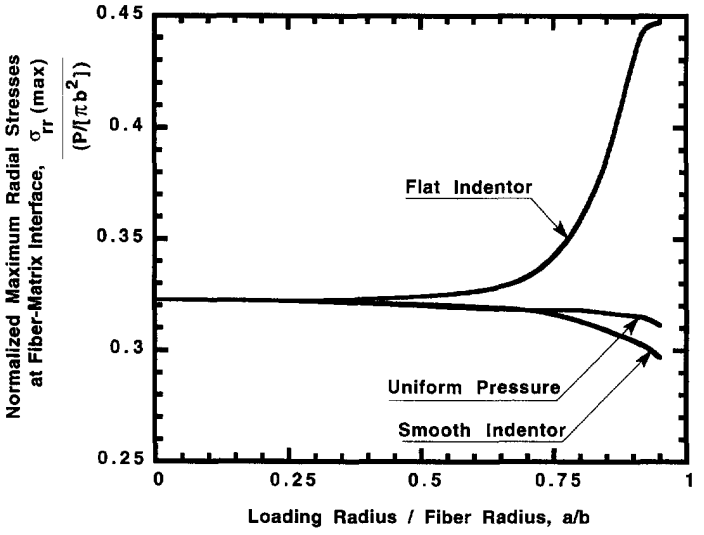

Fig. 4. Radial stress at interface as a function of the loading radius ratio (analytical model 1).

$$\lambda = \frac{Ev}{(1+v)(1-2v)} \tag{15a}$$

$$G = \frac{E}{2(1+v)} \tag{15b}$$

$$I_{ijk}(r,z,t) = \int_0^\infty \xi^k e^{-\xi z} J_i(\xi t) J_j(\xi r)\, d\xi \tag{15c}$$

and J is the Bessel's function of the first kind.

The integral in eqn (15c) is found in terms of elliptic integrals in Kaw and Pagano (1993), Eason *et al.* (1955), and Luk and Keer (1979).

Results. In Fig. 4, the maximum normalized interfacial radial stresses, $\sigma_{rr}(b,z)|_{max}/[P/(\pi b^2)]$, is plotted as a function of the normalized loading radius ratio, a/b. For loading radius ratios greater than 0.6 (that is $a/b > 0.6$), each indentor shape gives significantly different results. It is observed that the smooth indentor produced the smallest normalized stress and the flat indentor produced the highest normalized stress. The stresses due to the uniform pressure falls between the two extremes.

In Fig. 5, the maximum normalized interfacial shear stress, $\sigma_{rz}(b,z)|_{max}/[P/(\pi b^2)]$, is plotted as a function of normalized loading radius ratio, a/b. Similar to Fig. 4, for a loading radius ratio of $a/b > 0.6$, the results differ for the three types of indentors. Trends in the shear stress are similar to the trends in radial stress given in Fig. 4.

In Fig. 6, the maximum normalized hoop stress, $\sigma_{\theta\theta}(b,z)|_{max}/[P/(\pi b^2)]$, is plotted as a function of normalized loading radius ratio, a/b. For a loading radius ratio of $a/b > 0.75$, the effect of each indentor gives different results. The differences in hoop stresses due to the three indentors also follow the trends exhibited by the radial and shear stresses given in Figs 4 and 5, respectively.

In Fig. 7, the normalized axial displacement, $E_f u_z^f(b,0)/\{[P/(\pi b^2)]b\}$, is plotted as a function of the normalized loading radius, a/b. For a loading radius of $a/b > 0.6$, once again, the effect of the three types of indentors begins to vary.

From Figs 4–7, it is obvious that the stresses and displacements at the interface are influenced by indentor shape for loading radius ratios of 60% and more. Consequently, for indentors of radius greater than 60% of the fiber radius, analysis of the indentation test and interpretation of results from experimental indentation tests, should include the indentor shape. That is especially important for the commonly used flat indentor, which

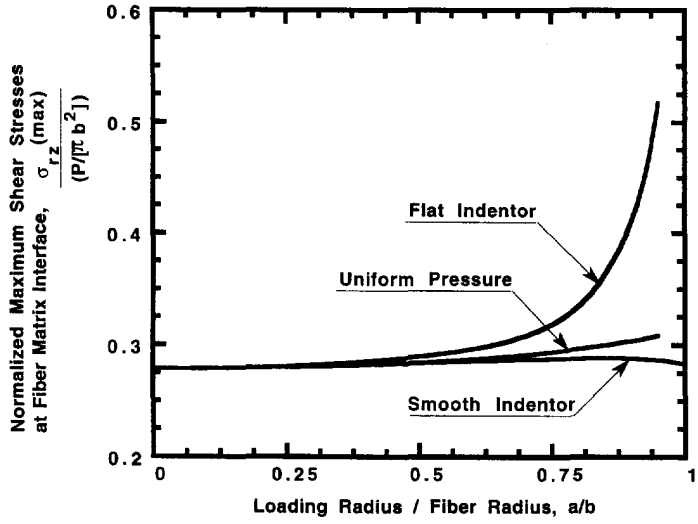

Fig. 5. Shear stress at interface as a function of the loading radius ratio (analytical model 1).

gives significantly different results than those from the other two indentor cases. Note that the equations are based on linear elasticity, and hence, these conclusions are valid for any indentor load, P.

Analytical model 2

The fiber-matrix bond is not "perfect" in ceramic matrix composites. Hence, an analytical model with friction in the interface following Coulomb's law is considered instead of a perfect bond. This model, which modifies analytical model 1 by including a frictional interface, is used to study the effect of indentor sizes and shapes on the load-displacement curves in an indentation test.

Geometry. Once again, the geometry of the model is shown in Fig. 3. A semi-infinite circular fiber of radius, b, is bonded to a half space of inner radius, b, and infinite outer radius. The elastic modulus of the fiber and matrix are assumed to be identical, that is, Young's modulus of the fiber and matrix is E, while Poisson's ratio is v.

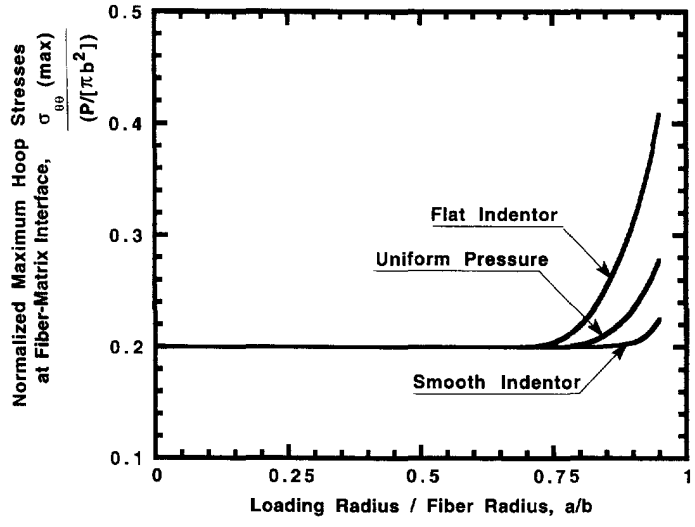

Fig. 6. Hoop stress at interface as a function of the loading radius ratio (analytical model 1).

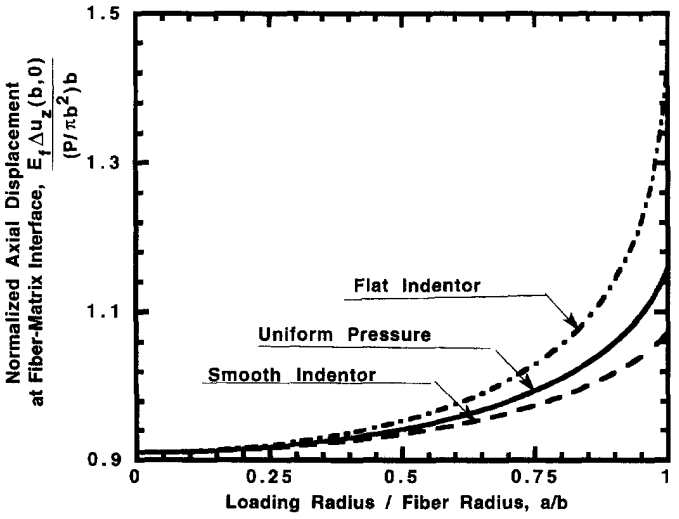

Fig. 7. Axial displacement at interface as a function of the loading radius ratio (analytical model 1).

Boundary conditions. The indentor load, P, is assumed to be applied monotonically increasing. The fiber-matrix interface (at $r = b$) is governed by Coulomb's friction law. Hence, at the interface, the open, slip or stick conditions are possible. The conditions in each of these zones are defined as follows:

Open zone:

$$\sigma_{rr}^{f}(b,z) = \sigma_{rr}^{m}(b,z) = 0, \quad 0 \leqslant z < L_0 \tag{16a}$$

$$\sigma_{rz}^{f}(b,z) = \sigma_{rz}^{m}(b,z) = 0, \quad 0 \leqslant z < L_0 \tag{16b}$$

subject to the open crack

$$u_r^{m}(b,z) - u_r^{f}(b,z) > 0, \quad 0 \leqslant z < L_0. \tag{17}$$

Slip zone:

$$\sigma_{rr}^{f}(b,z) = \sigma_{rr}^{m}(b,z), \quad L_0 < z < L_s \tag{18a}$$

$$\sigma_{rz}^{f}(b,z) = \sigma_{rz}^{m}(b,z), \quad L_0 < z < L_s \tag{18b}$$

$$u_r^{f}(b,z) = u_r^{m}(b,z), \quad L_0 < z < L_s \tag{18c}$$

$$|\sigma_{rz}^{f}(b,z)| = \mu|\sigma_{rr}^{f}(b,z)|, \quad L_0 < z < L_s \tag{18d}$$

subject to the compressive radial stress

$$\sigma_{rr}^{m}(b,z) < 0, \quad L_0 < z < L_s. \tag{19}$$

Stick zone:

$$\sigma_{rr}^{f}(b,z) = \sigma_{rr}^{m}(b,z), \quad L_s < z < \infty \tag{20a}$$

$$\sigma_{rz}^{f}(b,z) = \sigma_{rz}^{m}(b,z), \quad L_s < z < \infty \tag{20b}$$

$$u_r^{f}(b,z) = u_r^{m}(b,z), \quad L_s < z < \infty \tag{20c}$$

$$u_z^f(b,z) = u_z^m(b,z), \quad L_s < z < \infty \tag{20d}$$

subject to

$$\sigma_{rr}^f(b,z) < 0, \quad L_s < z < \infty \tag{21a}$$

$$|\sigma_{rz}^f(b,z)| < \mu|\sigma_{rr}^f(b,z)|, \quad L_s < z < \infty. \tag{21b}$$

In eqns (16)–(21), L_0 and $(L_s - L_0)$ represent the open and slip lengths, respectively. The other boundary conditions are the same as eqns (4)–(8) of analytical model 1. In addition, a radial stress of $-\sigma_0$ is assumed at the interface prior to application of the indentation load.

After solving the numerical problem, it is found that under the indentation load, there is no open zone, that is, $L_0 = 0$. Hence, the only two possibilities at the frictional interface for the problem are a slip zone and stick zone.

Method of analysis. The method of analysis follows that of Meda *et al.* (1993). The solution consists of superposing two solutions:

—a pressure $p(r)$ is applied on $0 < r < a < b$, $z = 0$ for a perfect bond at the interface, and
—prismatic circular dislocation loops are applied at the interface, $r = b$ such that it gives zero traction at $z = 0$.

These dislocations are applied axially (z-direction), such that only a discontinuous element at a frictional interface undergoes slip. The other stresses, σ_{rr} and σ_{rz}, and radial displacement, u_r are continuous across the interface.

Following the procedure in Meda *et al.* (1993), the solution to the problem is given by a single singular integral equation as

$$\sigma_{rz}^p(b,z) + \int_0^{L_s} \sigma_{rz}^d(b,z,z')\eta(z')\,\mathrm{d}z' = -\mu[\sigma_0 - \sigma_{rr}^p(b,z)] + \mu\int_0^{L_s} \sigma_{rr}^d(b,z,z')\eta(z')\,\mathrm{d}z' \tag{22}$$

where $\eta(z)$ is the dislocation density and is defined as

$$\eta(z) = \frac{\mathrm{d}}{\mathrm{d}z}[u_z^m(r,z+\varepsilon) - u_z^f(r,z-\varepsilon)] \tag{23}$$

The relevant stress components associated with a prismatic loop of unit Burgers vector in a half-space can be expressed as

$$\sigma_{rr}^d(r,z,z')e = [\sigma_{rr}^I(r,z,z') + \sigma_{rr}^{II}(r,z,z') + \sigma_{rr}^F(r,z,z')]e \tag{24}$$

$$\sigma_{rz}^d(r,z,z')e = [\sigma_{rz}^I(r,z,z') + \sigma_{rz}^{II}(r,z,z') + \sigma_{rz}^F(r,z,z')]e \tag{25}$$

where, the Burgers vector, e, is given by

$$e = \lim_{\varepsilon \to 0^+} [u_z(r,z'+\varepsilon) - u_z(r,z'-\varepsilon)] \neq 0, \quad 0 < r < b \tag{26}$$

and

$$\sigma_{rr}^I(r,z,z')e = \frac{eG}{2b(1-\nu)} I_{011}\left(1, \frac{|z-z'|}{b}, \frac{r}{b}\right) - \frac{|z-z'|}{b} I_{012}\left(1, \frac{|z-z'|}{b}, \frac{r}{b}\right)$$
$$- \frac{1-2\nu}{r/b} I_{110}\left(1, \frac{|z-z'|}{b}, \frac{r}{b}\right) + \frac{|z-z'|}{r} I_{111}\left(1, \frac{|z-z'|}{b}, \frac{r}{b}\right) \tag{27}$$

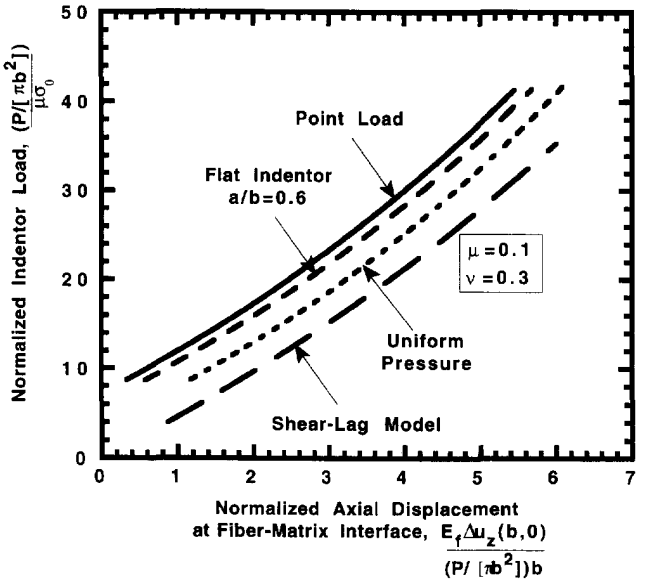

Fig. 8. Normalized indentor load as a function of normalized axial displacement (analytical model 2).

$$\sigma_{rr}^{II}(r,z,z') = -\sigma_{rr}^{I}(r,z,-z') \tag{28}$$

$$\sigma_{rz}^{I}(r,z,z')e = \frac{eG}{2b(1-\nu)}\frac{z-z'}{b}I_{112}\left(1,\frac{|z-z'|}{b},\frac{r}{b}\right) \tag{29}$$

$$\sigma_{rz}^{II}(r,z,z') = -\sigma_{rz}^{I}(r,z,-z') \tag{30}$$

$$\sigma_{rr}^{F}(r,z,z')e = \frac{-z'eG}{b^2(1-\nu)}\left[2I_{012}\left(1,\frac{z+z'}{b},\frac{r}{b}\right)-\frac{z}{b}I_{013}\left(1,\frac{z+z'}{b},\frac{r}{b}\right)\right.$$
$$\left.-\frac{2(1-\nu)}{r/b}I_{111}\left(1,\frac{z+z'}{b},\frac{r}{b}\right)+\frac{z}{b}I_{112}\left(1,\frac{z+z'}{b},\frac{r}{b}\right)\right] \tag{31}$$

$$\sigma_{rz}^{F}(r,z,z')e = \frac{z'eG}{b^2(1-\nu)}\left[I_{112}\left(1,\frac{z+z'}{b},\frac{r}{b}\right)-\frac{z}{b}I_{113}\left(1,\frac{z+z'}{b},\frac{r}{b}\right)\right] \tag{32}$$

$\sigma_{rr}^{p}(b,z)$ is given by substituting $r = b$ in eqn (11) and $\sigma_{rz}^{p}(b,z)$ is given by substituting $r = b$ in eqn (14). These two stresses are the normal and shear at the interface due to a circular patch of pressure, p, applied to the surface of the half-space. The integral equation is solved using collocation procedures (Meda *et al.*, 1993).

Results. The results herein were compared with those of Meda *et al.* (1993) for the case of uniform pressure with $a = b$. Excellent agreement between results were achieved, as expected, because the two solutions are, in essence, identical for this case.

In Fig. 8, the normalized indentor load, $[P/(\pi b^2)]/(\mu\sigma_0)$, is plotted as a function of normalized axial displacement, $E_f\Delta u_z(b,0)/\{[P/(\pi b^2)]b\}$, for various indentor shapes, where $\Delta u_z(b,0) = u_z^m(b^+,0) - u_z^f(b^-,0)$. A typical case with Poisson's ratio $\nu = 0.3$ and coefficient of friction $\mu = 0.1$ is assumed. The curve for uniform pressure case is the same as that of Meda *et al.* (1993). However, for a flat indentor with a typical radii of $a/b = 0.6$, these curves do not follow the same trend. The slip at the fiber-matrix interface decreases as the indentor radius is decreased. Even for an indentor radius of 80% of the fiber radius, the slip lengths are slightly less than in the uniform pressure case. It should be noted (figure not shown), however, that there is no significant difference in the indentor load versus slip

length for various indentor shapes and sizes. Hence, the approximation of the indentor load to a uniform pressure over the whole fiber diameter is reasonable only if one is relating the indentor load and slip length. But, it is not justified if one is relating indentor load, P, to the fiber and matrix displacement difference at the top surface ($z = 0$), $\Delta u_z(b, 0)$.

Also shown in Fig. 8 is the load-displacement curve obtained by the shear-lag analysis model (Shetty, 1988). Since load-displacement curves are regressed to analytical models for obtaining the interface parameters, coefficient of friction and residual stresses, accurate analytical models become vital in experimental characterization of composites.

FINITE ELEMENT MODEL

Analytical models for a finite geometry and dissimilar fiber and matrix properties of an indentation test are cumbersome and possibly untractable. Hence, a finite element model (FEM) is used to incorporate these features in an indentation test. The FEM presented in this study is used to study the effects of the following on the indentation test:

—radius of the hole through which fiber is pushed in during the indentation test,
—relative elastic moduli of the fiber and the matrix,
—sizes and shapes of the indentors, and
—material symmetry of the fiber.

For each case, an axisymmetric model of the composite was generated using the finite element software, NIKE-2D (1991).

Geometry and mesh

The mesh of the finite element model was generated using the non-commercial finite element code NIKE-2D (1991) with MAZE and ORION, as the pre-processor and post-processor, respectively. The mesh is generated in the rz-plane and consists of 3400 axi-symmetric rectangular elements. The fiber, which occupies the domain $0 \leqslant z \leqslant 50b$ and $0 \leqslant r \leqslant b$, where b is the radius of the fiber, consists of 500 elements. The matrix, which occupies a domain $0 \leqslant z \leqslant 50b$ and $b \leqslant r \leqslant 50b$, is made up of two parts. The first part consisting of 500 elements has $b \leqslant r \leqslant 2b$ as the domain and the second part consisting of 2400 elements has $2b \leqslant r \leqslant 50b$, as the domain.

Boundary conditions

The interface between the fiber and the matrix follows the Coulomb friction law as follows:

Open zone:

$$\sigma_{rr}^f(b, z) = \sigma_{rr}^m(b, z) = 0, \quad 0 \leqslant z < L_0 \tag{33a}$$

$$\sigma_{rz}^f(b, z) = \sigma_{rz}^m(b, z) = 0, \quad 0 \leqslant z < L_0 \tag{33b}$$

subject to the open crack

$$u_r^m(b, z) - u_r^f(b, z) > 0, \quad 0 \leqslant z < L_0. \tag{34}$$

Slip zone:

$$\sigma_{rr}^f(b, z) = \sigma_{rr}^m(b, z), \quad L_0 < z < L_s \tag{35a}$$

$$\sigma_{rz}^f(b, z) = \sigma_{rz}^m(b, z), \quad L_0 < z < L_s \tag{35b}$$

$$u_r^f(b, z) = u_r^m(b, z), \quad L_0 < z < L_s \tag{35c}$$

$$|\sigma_{rz}^{f}(b,z)| = \mu|\sigma_{rr}^{f}(b,z)|, \quad L_0 < z < L_s \tag{35d}$$

subject to the compressive radial stress

$$\sigma_{rr}^{m}(b,z) < 0, \quad L_0 < z < L_s. \tag{36}$$

Stick zone:

$$\sigma_{rr}^{f}(b,z) = \sigma_{rr}^{m}(b,z), \quad L_s < z < 50b \tag{37a}$$

$$\sigma_{rz}^{f}(b,z) = \sigma_{rz}^{m}(b,z), \quad L_s < z < 50b \tag{37b}$$

$$u_r^{f}(b,z) = u_r^{m}(b,z), \quad L_s < z < 50b \tag{37c}$$

$$u_z^{f}(b,z) = u_z^{m}(b,z), \quad L_s < z < 50b \tag{37d}$$

subject to

$$\sigma_{rr}^{f}(b,z) < 0, \quad L_s < z < 50b \tag{38a}$$

$$|\sigma_{rz}^{f}(b,z)| < \mu|\sigma_{rr}^{f}(b,z)|, \quad L_s < z < 50b \tag{38b}$$

At $z = 0$, only the fiber is subjected to a pressure, $p(r)$, over a radius, a, that is,

$$\sigma_{zz}^{f}(r,0) = -p(r), \quad 0 < r < a \tag{39a}$$

$$\sigma_{zz}^{f}(r,0) = 0, \quad a < r < b \tag{39b}$$

$$\sigma_{zz}^{m}(r,0) = 0, \quad b < r < 50b \tag{39c}$$

Furthermore, on the surface ($z = 0$), the shear stress is zero, that is,

$$\sigma_{rz}^{f}(r,0) = 0, \quad 0 \leqslant r \leqslant b \tag{40a}$$

$$\sigma_{rz}^{m}(r,0) = 0, \quad b \leqslant r \leqslant 50b \tag{40b}$$

Since the model is axisymmetric, the mesh is generated only for one half of the composite. Hence, the fiber is fixed in the r direction at $r = 0$ and $0 \leqslant z \leqslant 50b$, as shown in Fig. 9.

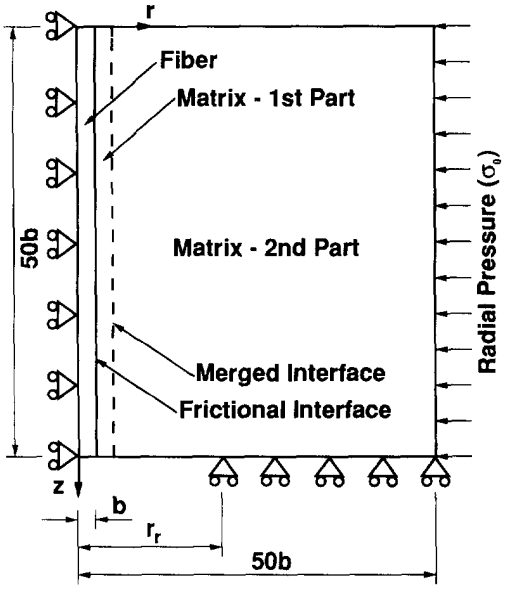

Fig. 9. Finite element mesh, boundary conditions, and external pressure acting on the matrix for the finite element analysis (FEM models).

These conditions translate as:

$$u_r^f(0,z) = 0, \quad 0 < z < 50b \tag{41a}$$

$$\sigma_{rz}^f(0,z) = 0, \quad 0 < z < 50b \tag{41b}$$

Furthermore, the matrix is fixed in the z direction at $z = 50b$, $r_r \leqslant r \leqslant 50b$, as shown in Fig. 9, where r_r is the radius of the push through hole. The fiber is not restrained at the bottom at $z = 50b$ and the matrix is also not restrained at $z = 50b$, $0 \leqslant r \leqslant r_r$ to simulate the hole for the indentation test. These conditions translate as:

$$\sigma_{zz}^f(r,50b) = 0, \quad 0 < r < b \tag{42a}$$

$$\sigma_{rz}^f(r,50b) = 0, \quad 0 < r < b \tag{42b}$$

$$\sigma_{zz}^m(r,50b) = 0, \quad b < r < r_r \tag{42c}$$

$$u_z^m(r,50b) = 0, \quad r_r < r < 50b \tag{42d}$$

$$\sigma_{rz}^m(r,50b) = 0, \quad b < r < 50b \tag{42e}$$

To simulate the interfacial radial stress due to thermal expansion mismatch during processing, a temperature difference between processing and operating temperatures could be applied. This temperature difference develops interfacial stresses due to thermal expansion mismatch between the fiber and matrix. However, since the fiber is not constrained in the axial direction, a difference in the lengths of the matrix and the fiber would develop, resulting in a difference in axial displacements between the fiber and the matrix at the surface prior to subjecting the composite to an indentation load.

Because of the above simulation problem, it was decided to simulate the residual thermal stresses at the interface by applying an external radial pressure rather than from a temperature mismatch. The resulting conditions translate as:

$$\sigma_{rr}^m(50b,z) = -\sigma_0, \quad 0 < z < 50b \tag{43a}$$

$$\sigma_{rz}^m(50b,z) = 0, \quad 0 < z < 50b \tag{43b}$$

where a typical value, based on thermal expansion mismatch, elastic moduli and temperature differences in the SI, $\sigma_0 = 0.207 \times 10^7$ is used for all models. The radial pressure applied to the matrix, to simulate the interfacial residual stresses, is shown in Fig. 9. Although this is an approximate way of including residual stresses, the main purpose of this paper is to isolate the effects of the extrinsic factors.

Comparison of FEM results with analytical predictions

Since further calculations in this study are based on the mesh generated using finite elements, it was deemed necessary to establish the accuracy of the finite element method and the generated mesh. To accomplish this, the displacements at the fiber-matrix interface on the surface, $r = b$ and $z = 0$, for the case of identical elastic moduli with a frictional interface and uniform pressure acting on the fiber were compared with those of Meda *et al.* (1993). The results verified within a 5% difference. The results were also compared with the analytical results for both a uniform pressure ($a/b = 0.4$) and a flat indentor ($a/b = 0.4$) acting on the fiber with a perfect interface. Again, the results matched satisfactorily, within a 5% difference. The above comparisons suggest that the mesh generated is refined enough and that the finite element code is dependably accurate.

FEM model 1

A circular fiber of radius b (1 unit for the present case) embedded in a circular matrix ($r = 50b$ units for this case) is placed on a circular hole. The fiber and the matrix are

assumed to have the same elastic modulus of 1.0×10^9, and Poisson's ratio of 0.3. The interface follows the Coulomb friction law with a coefficient of friction of 0.1. An arbitrary point load is applied at the center of the fiber. Keeping this load constant, the radius of the hole is varied by fixing the nodes in the z-direction from the desired radius, $r = r_r$ to the end of the matrix, $r = 50b$ at $z = 50b$ [refer to eqns (42d,e)]. In particular, the radius of the push through hole is varied, from close to the interface ($r_r = 1.2b$) to close to the end ($r_r = 40b$) of the matrix, to study the effect of the radius of the hole, r_r, during the indentation tests.

Results. It is found that the load-displacement curve varied insignificantly with a change in the radius of the push through hole. Since the variation is insignificant, the figure has been omitted.

FEM model 2

This model is similar to FEM model 1 discussed above. However, the radius of the hole at the bottom support is fixed at $r_r = 10b$ for all cases in this model and the loading on the fiber is varied.

The fiber is subjected to a pressure, $p(r)$, over a radius, a, that is,

$$\sigma_{zz}^{f}(r, 0) = -p(r), \quad 0 < r < a < b \tag{44}$$

where, the pressure, $p(r)$, is arbitrary. Since the loads can be applied only at the nodes, the ratio of the loading radius to the radius of the fiber, a/b, has been restricted to an increment of the element size ($0.2b$ in this model). The ratio a/b is varied from 0.2 to 1.0 for the case of a uniform pressure and from 0.2 to 0.8 for the case of a flat indentor.

The fiber is subjected to a point load, a uniform pressure and the resulting pressure distribution from the flat indentor. The uniform pressure distribution is made to approximate an indentor load where the pressure, $p(r)$, is assumed to be of the form given by eqn (8), whereas, the pressure distribution in the case of the flat indentor is given by eqn (6a). The overall load, P, applied to the indentor is given by eqn (7).

Results. This model was simulated to study the effect of the shape and size of the indentor during the indentation test. Three different indentors, namely, point load, uniform pressure and flat indentor, were used in this model.

In Fig. 10, the normalized indentor load, $[P/(\pi b^2)]/(\mu\sigma_0)$, is plotted against the normalized relative axial displacement between fiber-matrix at the interface, $E_f \Delta u_z(b, 0)/$

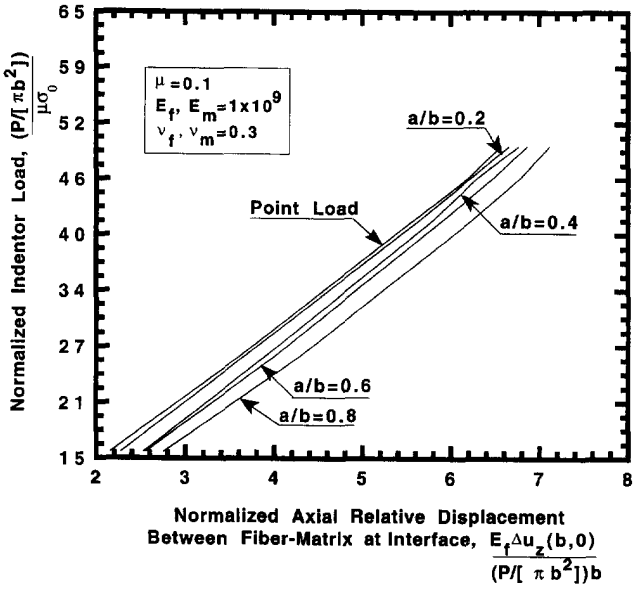

Fig. 10. Indentor load as a function of axial relative displacement between fiber-matrix at interface for flat indentor (FEM model 1).

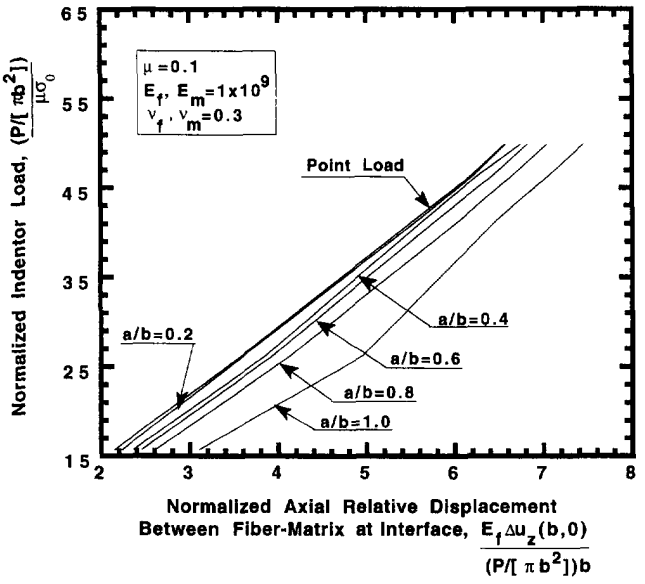

Fig. 11. Indentor load as a function of axial relative between fiber-matrix at interface for uniform pressure (FEM model 2).

$\{[P/(\pi b^2)]b\}$, for the point load and flat indentor cases. The curves clearly illustrate the effect of indentation pressure on displacements. For the same indentor load, the normalized relative axial displacement between fiber-matrix at the interface increased with an increase in the loading radius ratio, a/b as shown in Fig. 10.

Figure 11 shows the normalized indentor load, $[P/(\pi b^2)]/(\mu\sigma_0)$, as a function of the normalized relative axial displacement between fiber-matrix at the interface, $E_f\Delta u_z(b,0)/\{[P/(\pi b^2)]b\}$, for the point load and uniform pressure cases. In this case it is observed that for the same indentor load, the normalized relative axial displacement between fiber-matrix at the interface increases with an increase in the loading radius ratio, a/b.

To facilitate an easy and direct comparison between the uniform pressure and the flat indentor, both cases are shown in Fig. 12, for two loading radii. Figure 12 clearly shows that the normalized relative axial displacement between fiber-matrix at the interface in the

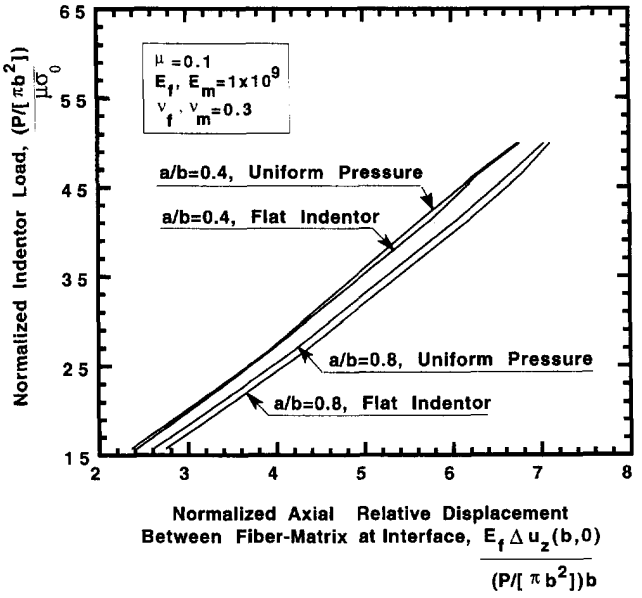

Fig. 12. Indentor load as a function of axial relative between fiber-matrix at interface for flat indentor and uniform pressure (FEM models 1 and 2).

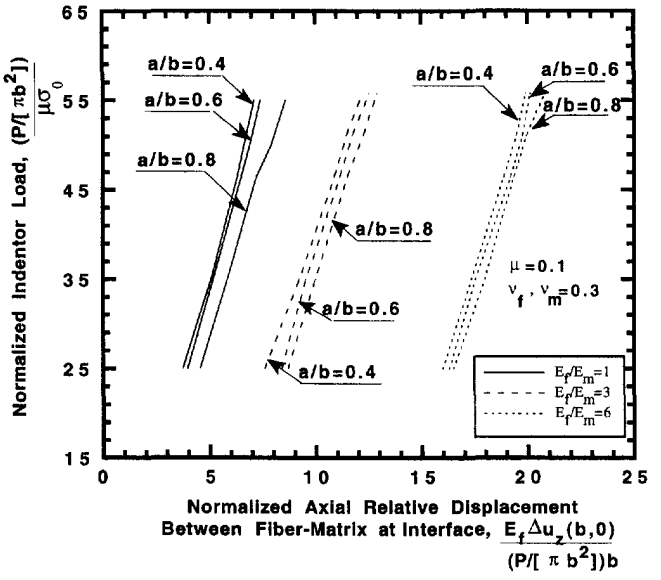

Fig. 13. Indentor load as a function of axial relative displacement between fiber-matrix at interface for different Young's moduli ratios (FEM model 3).

flat indentor case is always more than that caused by the uniform pressure for the same indentor load.

FEM model 3

This model is also similar to the two previous models discussed. The radius of the push through hole is fixed at $r_r = 10b$ and a flat indentor with pressure, $p(r)$, and ratio $a/b = 0.8$ is used. Young's modulus of the fiber is varied to study the effect of the Young's modulus on the indentation test.

Three different cases have been studied in this model. The ratio of Young's modulus of the fiber to Young's modulus of the matrix is different for all three cases. The first case is for a similar Young's modulus, $E_f/E_m = 1$. In the second case, the ratio of the Young's modulus of the fiber to the matrix is 3, (i.e. $E_f/E_m = 3$) and the third case represents a modulus ratio of 6, (i.e. $E_f/E_m = 6$).

Results. To study the effect of Young's modulus on the indentation test, the simulation has been performed with a flat indentor of radii 0.4, 0.6 and 0.8. Figure 13 illustrates the effect of the ratio of Young's moduli (E_f/E_m) on the indentation test. The relative displacement between the fiber and matrix was found to increase with an increase in the ratio of Young's moduli.

FEM model 4

This model is simulated to examine the effects of transverse isotropy of the fiber on the load-displacement curve. Model 4 is similar to the three previous models, wherein the radius of the push through hole is fixed at $r_r = 10b$ and the fiber is pushed with a flat indentor with pressure, $p(r)$, for a ratio of $a/b = 0.8$. The properties of the fiber are varied from an isotropic state to a transversely isotropic state. Five cases are studied in this model. The first case deals with the fiber being isotropic. The properties of the fiber have been changed to transversely isotropic case in four equal steps as shown in Table 1. Once again, the normalized relative axial displacement between fiber-matrix at the interface is studied and plotted vs the load to study the effect of the isotropic and transversely isotropic fiber.

Results. Figure 14 clearly illustrates that there is significantly more relative axial displacement between fiber-matrix at the interface for an isotropic fiber compared to a transversely isotropic fiber. Furthermore, the relative displacement rapidly decreases as the

Table 1. Material properties of fiber for transition from isotropic to transversely isotropic

Run	Description	$E_f^r = E_f^\theta$ (GPa)	E_f^z (GPa)	$\nu_f^{r\theta}$	$\nu_f^{rz} = \nu_f^{\theta z}$	E_m (GPa)	ν_m
1	Isotropic fiber	234.97	234.97	0.2000	0.2	26.25	0.2
2	Transition step 1	179.72	234.97	0.2125	0.2	26.25	0.2
3	Transition step 2	124.48	234.97	0.2250	0.2	26.25	0.2
4	Transition step 3	69.24	234.97	0.2375	0.2	26.25	0.2
5	Transversely Isotropic fiber	13.99	234.97	0.2500	0.2	26.25	0.2

property of the fiber approaches the transversely isotropic properties. It is seen that the difference in the relative axial displacement between fiber-matrix at the interface from the isotropic case to the first and the second transition steps is small. The relative displacement from the second transition step to the third is larger, while the relative displacement from the third transition step to the transversely isotropic case, is very large.

CONCLUSIONS

The effect of the extrinsic and intrinsic factors on the interface has been studied using the indentation test. The various extrinsic factors studied included the radius of the hole of the support, and shape and size of the indentors. The intrinsic factors studied were various ratios of fiber to matrix Young's modulus and the transition from an isotropic fiber to a transversely isotropic fiber. The conclusions drawn from the studies are:

1. the indentation test is not affected by the radius of the hole through which the fiber is pushed. Thus, the indentation test can be performed with any convenient radius of this hole;
2. the displacements, slip lengths and stresses for the flat indentor case are more than that in the uniform pressure case. Moreover, the normalized relative axial displacement between fiber-matrix at the interface increases as the size/radius of the indentor increases. Hence, the shape of the indentors, especially, with loading radius ratios of 60% or more of the fiber radius, should be dealt with differently in the analysis of indentation tests;

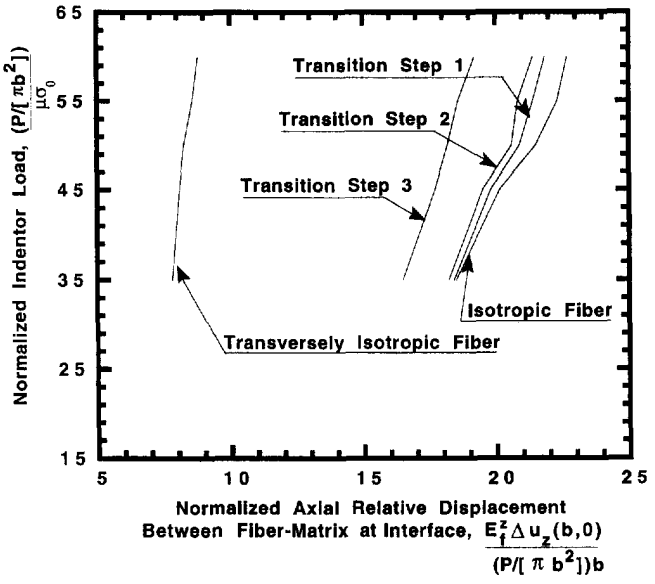

Fig. 14. Indentor load as a function of axial relative displacement between fiber-matrix at interface for a transversely isotropic fiber (FEM model 4).

3. the relative displacement between the fiber and matrix increases as the ratio of Young's modulus between the fiber and matrix increases. It is also found that the relative displacement between the fiber and matrix increases with an increase in the radius of the indentor;
4. the normalized relative axial displacement between fiber-matrix at the interface in the transversely isotropic case are far less than those in the isotropic case. As the material symmetry of the fiber approaches isotropic, the displacements get larger and uniform. Therefore, the approximation of transversely isotropic fibers as isotropic is not suitable.

Acknowledgements—This work was supported by AFOSR, Bolling AFB, Washington, DC via Grant no. F49620-95-1-0164. The encouragement of the AFOSR grant monitor, Dr. Walter Jones, is deeply appreciated. The authors would also like to thank Lawrence Livermore National Laboratory, CA for the use of the NIKE-2D finite element software in agreement with license to University of South Florida, Tampa and for the technical help given by Dr. Bruce Engelman and Dr. Ed Zywicz. The authors would like to thank Prof. Paul Steif and Dr. Gautam Meda of Carnegie Mellon University, PA for extensive discussions and for providing comparative numerical results. A version of this paper is printed in the Proceedings of Symposium on Micromechanics and Constitutive Modelling of Composites Materials, ASME Summer Annual Meeting, June 28–30, 1995, UCLA.

REFERENCES

Bright, J. D., Danchaivijit, S. and Shetty, D. K. (1991). Interfacial sliding friction in silicon carbide-borosilicate glass composites: a comparison of pullout and pushout tests. *J. Am. Ceramic Soc.* **74,** 115–122.

Curtin, W. A., Eldrige, J. I. and Srinivasan, G. V. (1993). Push-in tests on a new silicon carbide/reaction silicon carbide ceramic matrix composite. *J. Am. Ceramic Soc.* **76,** 2300–2304.

Eason, G., Noble, B. and Sneddon, I. N. (1955). On certain integrals of Lipschitz-Hankel type involving products of Bessel functions. *Philos. Trans. R. Soc.* **A247,** 529–551.

Faber, K. T., Advani, S. H., Lee, J. K. and Jinn, J. T. (1986). Frictional stress evaluation along the fiber-matrix interface in ceramic matrix composites. *J. Am. Ceramic Soc.* **69,** C208–C209.

Grande, D. H., Mandell, J. F. and Hong, K. C. C. (1988). Fiber-matrix bond strength studies of glass, ceramic and metal matrix composites. *J. Mat. Sci.* **23,** 311–328.

Kaw, A. K. and Pagano, N. J. (1993). Axisymmetric thermoelastic response of a composite cylinder containing an annular crack. *J. Comp. Mat.* **27,** 540–571.

Koss, D. A., Hellmann, J. R. and Kallas, M. N. (1993). Fiber pushout and interfacial shear in metal-matrix composites. *J. Mat.* **45,** 34–37.

Lawrence, C. W. and Derby, B. (1993). Interfacial frictional shear stresses in ceramic matrix composites. *Ceramic Engng Sci. Proc.* **14,** 139–146.

Luk, V. K. and Keer, L. M. (1979). Stress analysis for an elastic half space containing an axially-loaded rigid cylindrical rod. *Int. J. Solids Structures* **15,** 805–827.

Marshall, D. B. (1984). An indentation method for measuring matrix fiber frictional stresses in ceramic composites. *J. Am. Ceramic Soc.* **67,** C259–C260.

Meda, G., Hoysan, S. F. and Steif, P. S. (1993). The effect of fiber Poisson expansion in micro-indentation tests. *J. Appl. Mech.* **60,** 986–991.

NIKE-2D. (1991). *A Nonlinear, Implicit, Two-Dimensional Finite Element Code for Solid Mechanics-User Manual*, Lawrence Livermore National Laboratory, Livermore, CA.

Shetty, D. K. (1988). Shear-lag analysis of fiber pushout (indentation) test for estimating interfacial frictional stress in ceramic-matrix composites. *J. Am. Ceramic Soc.* **71,** C107–C109.

Shirazi-Adi, A. (1992). Finite element stress analysis of a push-in test part I: fixed interface using stress compatible elements. *J. Biomechanical Engng* **114,** 111–118.

Sneddon, I. N. (1951). *Fourier Transforms*, McGraw-Hill, New York.

APPENDIX A: PLANAR INDENTATION MODEL (ANALYTICAL MODEL 3)

Many researchers model the indentation test using planar models. In this appendix, a comparison is made between planar and axisymmetric models. An equivalent planar geometry of Model 1 is taken. A semi-infinite fiber strip is bonded perfectly to two quarter planes of identical elastic moduli as shown in Fig. A1. An arbitrary pressure, symmetric about the z-axis is applied over an arbitrary area on the fiber. The maximum interfacial stresses are compared with the equivalent axisymmetric problem to determine the difference between results between the planar and axisymmetric models.

Geometry

The geometry of the model is shown in Fig. A1. A semi-infinite strip of width, $2B$, is bonded to two quarter-planes at $x = \pm B$. In order to differentiate between the axisymmetric and planar models, capital notations have been used in the planar model and the radial coordinate, r, has been replaced with x. Young's modulus and Poisson's ratio of the fiber and matrix are equal and are denoted as E and ν, respectively.

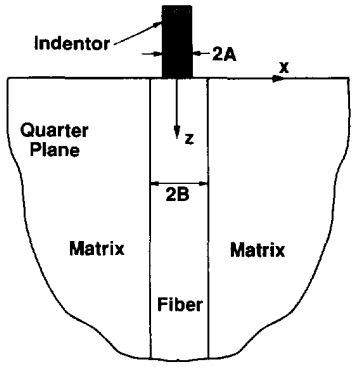

Fig. A1. Planar model of the indentation test (analytical model 3).

Boundary conditions

The fiber and matrix are perfectly bonded, that is,

$$u_x^f(B,z) = u_x^m(B,z), \quad 0 < z < \infty \tag{A.1a}$$

$$u_z^f(B,z) = u_z^m(B,z), \quad 0 < z < \infty \tag{A.1b}$$

$$\sigma_{xx}^f(B,z) = \sigma_{xx}^m(B,z), \quad 0 < z < \infty \tag{A.2a}$$

$$\sigma_{xz}^f(B,z) = \sigma_{xz}^m(B,z), \quad 0 < z < \infty \tag{A.2b}$$

The fiber is subjected to a pressure, $p(x)$, over a length A, that is,

$$\sigma_{zz}^f(0,z) = -p(x), \quad 0 \leqslant |x| < A \tag{A.3}$$

The pressure, $p(x)$, the load, P, and the loading length, A, are arbitrary. The pressure distribution, $p(x)$, for common indentors is taken as

$$p(x) = \frac{P}{\pi\sqrt{A^2 - x^2}}, \quad 0 < |x| < A \qquad \text{(flat indentor)} \tag{A.4}$$

$$p(x) = \frac{2P}{\pi A^2}\sqrt{A^2 - x^2}, \quad 0 < |x| < A \quad \text{(smooth indentor)} \tag{A.5}$$

The uniform pressure assumption is of the form

$$p(x) = \frac{P}{2A}, \quad 0 < |x| < A \quad \text{(uniform pressure)} \tag{A.6}$$

where P = load/unit width. On the surface $z = 0$, the shear stress is

$$\sigma_{xz}^f(x,0) = 0, \quad 0 < |x| < B \tag{A.7a}$$

$$\sigma_{xz}^m(x,0) = 0, \quad B < |x| < \infty \tag{A.7b}$$

Method of analysis

This problem is solved by using a Fourier Transform solution for a half-plane. The displacements are given by

$$u_x(x,z) = \frac{2}{\pi}\int_0^\infty \left(z + \frac{\kappa+1}{2\eta}\right) f(\eta) e^{-\eta z}\cos(\eta x)\,d\eta \tag{A.8}$$

$$u_z(x,z) = \frac{2}{\pi}\int_0^\infty \left(z + \frac{1-\kappa}{2\eta}\right) f(\eta) e^{-\eta z}\sin(\eta x)\,d\eta \tag{A.9}$$

where $\kappa = 3 - 4\nu$ for a plane strain assumption and the stresses are given by

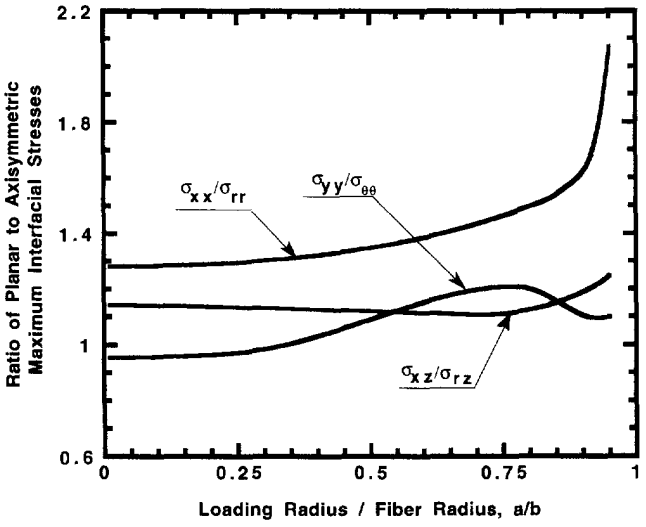

Fig. A2. Ratio of the stresses of planar and axisymmetric models for the flat indentor as a function of the loading radius ratio (analytical model 3).

$$\sigma_{xx}(x,z) = -\frac{4G}{\pi}\int_0^{\infty}(1+\eta z)f(\eta)e^{-\eta z}\cos(\eta x)\,d\eta \tag{A.10}$$

$$\sigma_{xz}(x,z) = -\frac{4G}{\pi}\int_0^{\infty}\eta z f(\eta)e^{-\eta z}\sin(\eta x)\,d\eta \tag{A.11}$$

$$\sigma_{zz}(x,z) = \frac{4G}{\pi}\int_0^{\infty}(\eta z-1)f(\eta)e^{-\eta z}\cos(\eta x)\,d\eta \tag{A.12}$$

where

$$f(\eta) = -\frac{P}{4AG}\frac{\sin(\eta a)}{\eta} \quad \text{(uniform pressure)} \tag{A.13a}$$

$$= -\frac{P}{4G}J_0(\eta a) \quad \text{(flat indentor)} \tag{A.13b}$$

$$= -\frac{P}{4G\eta a}J_1(\eta a) \quad \text{(smooth indentor)} \tag{A.13c}$$

Furthermore, for a plane strain assumption,

$$\sigma_{yy}(x,z) = \nu[\sigma_{xx}(x,z)+\sigma_{zz}(x,z)] \tag{A.14}$$

The stresses for the uniform pressure case can be found in closed form in Timoshenko and Goodier (1985).

Results

In Fig. A2, the ratio of interfacial stresses for the axisymmetric and planar models is given for the flat indentor case only, since it is used most often in indentation tests. The same loads are applied over an equal radius (axisymmetric) and loading width (planar case), that is,

$$P = \int_0^{2\pi}\int_0^{a} p(r)r\,dr\,d\theta \quad \text{(axisymmetric)} \tag{A.15a}$$

$$P = \int_{-A}^{A} p(x)\,dx \quad \text{(planar)} \tag{A.15b}$$

It can be seen from Fig. A2 that for a normalized loading radius ratio greater than 0.25, the maximum interfacial stresses for the planar case are greater than the axisymmetric case. Generally, the stress ratios increase with an increase in normalized loading radius, especially for a radial stress ratio which increases rapidly when the normalized loading radius ratio approaches 1.